The lunar solid inner core and the mantle overturn

Arthur Briaud, Clément Ganino, Agnès Fienga, Anthony Mémin, Nicolas Rambaux

Article

The lunar solid inner core and the mantle overturn

https://doi.org/10.1038/s41586-023-05935-7

Received: 19 May 2022

Accepted: 8 March 2023

Published online: 3 May 2023

Check for updates

Arthur Briaud[1]✉, Clément Ganino[1], Agnès Fienga[1,2]✉, Anthony Mémin[1] & Nicolas Rambaux[2]

Seismological models from Apollo missions provided the first records of the Moon inner structure with a decrease in seismic wave velocities at the core–mantle boundary[1–3]. The resolution of these records prevents a strict detection of a putative lunar solid inner core and the impact of the lunar mantle overturn in the lowest part of the Moon is still discussed[4–7]. Here we combine geophysical and geodesic constraints from Monte Carlo exploration and thermodynamical simulations for different Moon internal structures to show that only models with a low viscosity zone enriched in ilmenite and an inner core present densities deduced from thermodynamic constraints compatible with densities deduced from tidal deformations. We thus obtain strong indications in favour of the lunar mantle overturn scenario and, in this context, demonstrate the existence of the lunar inner core with a radius of 258 ± 40 km and density 7,822 ± 1,615 kg m^{-3}. Our results question the evolution of the Moon magnetic field thanks to its demonstration of the existence of the inner core and support a global mantle overturn scenario that brings substantial insights on the timeline of the lunar bombardment in the first billion years of the Solar System[8].

The lunar mantle overturn has been proposed to explain the abundances of TiO_2, FeO and heat-producing elements (U, Th and K) in the source region of lunar basalts and the sequestration of highly siderophile elements (HSEs) and iron–sulfur in the lunar mantle[8–11]. Rocks containing iron–titanium oxide are called ilmenite-bearing cumulates (IBCs) and form during the slow cooling of lunar magma ocean. These IBCs are concentrated through the process of magmatic segregation[12]. The IBCs would contain ilmenite, a dense iron–titanium oxide ($FeTiO_3$) forming a solid solution with geikielite ($MgTiO_3$)[13]. The partial melt of the IBCs is denser and less buoyant than the surrounding mantle. Hence, the IBCs may sink through the mantle by gravitational instability and stabilize at the core–mantle boundary (CMB) of the Moon[6]. This event is invoked to drive the deep lunar mantle overturn, hereafter called DLMO (see Methods). These IBCs tracers of the DLMO can be identified by their lower viscosity and lower solidus temperature in comparison with other lunar mantle material[6]. Furthermore, the existence of a solid inner core is not clearly demonstrated, as the seismic profiles obtained with the Apollo missions can be explained equally well with or without an inner core[2,3]; see also ref. 14.

Here we combine lunar tidal deformations of degree 2 Love numbers, frequency-dependent quality factors, mass and the moment of inertia to estimate the thicknesses, densities and viscosities of a layered Moon with or without an inner core. To compute the tidal deformations, we use the semi-analytical code ALMA[15] adapted to the tidal forcing[16] and using 1D profiles of density, rigidity and viscosity as input parameters.

Geophysical and geodesic constraints

On the basis of random-walk Monte Carlo samplings for these quantities and over intervals corresponding to state-of-the-art estimations, we select models that are consistent at 2σ with the published geophysical constraints (see Methods for more details). These observational constraints are the total mass of the Moon, its moment of inertia and its tidal deformation (characterized by parameters k_2, h_2 and the monthly and yearly quality factors) at 2σ uncertainties of the published estimations. In the case of several estimations (as for h_2 with the lunar laser ranging and altimetry determinations), we consider as uncertainty the largest interval encompassing the different published values.

The selected profiles given in Table 1 represent 0.12% of a total of 120,000 simulations. The crustal thickness is fixed according to the GRAIL average crustal model with a density of 2,649 kg m^{-3}, representative to an average crustal bulk porosity of 9.5% (ref. 17). For the mantle, its density determination is part of the random-walk Monte Carlo sampling but only to keep the balance of the global mass. Furthermore, we verified that the deduced mantle densities are consistent with the S-wave velocity models of refs. 2,3, as given in Extended Data Table 3. Finally, we define the inner core with a fixed rigidity and as purely elastic with infinite viscosity, in contrast with the outer core, which is a Newtonian fluid with no rigidity and a non-zero viscosity (see Extended Data Table 3). In Table 1, the radii of the different layers are well constrained as their 2σ uncertainties and are usually smaller than 9.5%, except for the radius of the inner core, for which the dispersion reaches 15.5%. In the hypothesis of a Moon without an inner core, our estimate for the density of the viscous core is 7,757 ± 1,749 kg m^{-3}. This density is on average, slightly lower than that expected for a purely metal-rich core. It rather indicates an alloy of iron with lighter elements, similar to a liquid Fe-S at 0.1% of sulfide content despite the wide range of uncertainty[18]. The large viscosity ($10^{18.45 \pm 1.85}$ Pa s) we derived for the models without an inner core allows rejecting the hypothesis of an entirely inviscid fluid core (for example, refs. 2,19).

[1]Université Côte d'Azur, Observatoire de la Côte d'Azur, CNRS, Géoazur, Valbonne, France. [2]IMCCE, Observatoire de Paris, Sorbonne Université, PSL University, CNRS, Paris, France.
✉e-mail: briaud@geoazur.unice.fr; agnes.fienga@oca.eu

Table 1 | Lunar 1D profile characteristics deduced from this study

Models	Layer	Radius (km)	Density (kg m^{-3})	Viscosity, $\log_{10}$ (Pa s)
Without inner core	Crust	1,737.1	2,649	–
	Mantle	1,698.6	3,362±2	21.00
	LVZ	545±35	3,884±300	16.99±1.22
	Core	315±30	7,757±1,749	18.45±1.85
With inner core	Crust	1,737.1	2,649	–
	Mantle	1,698.6	3,362±2	21.00
	LVZ	560±34	3,559±94	17.98±1.06
	Outer core	362±15	5,025±604	16.92±0.08
	Inner core	258±40	7,822±1,615	–

Internal Moon parameters obtained after the random-walk Monte Carlo sampling for the profiles with and without an inner core. The errors are given at 2σ. The quantities given without uncertainties are kept fixed.

For the hypothesis of a Moon having both a viscous core and a solid inner core, the density and the viscosity of the outer core as given in Table 1 are even smaller (5,025 ± 604 kg m^{-3} and $10^{16.92\pm0.08}$ Pa s, respectively). Despite the wide dispersion in densities, this is compatible with a differentiation scenario in which the heavier elements sunk to the solid inner core and only lighter elements remain in the outer viscous core. The density we obtained for the viscous core thus indicates that the sulfide content could reach up to 0.4 S content (at %)[18]. By contrast, we obtain, on average, a slightly higher density of the solid inner core (7,822 ± 1,615 kg m^{-3}), in comparison with the density of the single viscous core (7,757 ± 1,749 kg m^{-3}). Furthermore, the outer core radius is compatible with the lunar laser ranging estimation of 381 ± 12 km (ref. 20). For the previous constraints on the lunar inner core, we derived similar thickness (258 ± 40 km) and density (7,822 ± 1,615 kg m^{-3}) as those obtained by Weber et al.[2], who proposed a 240-km-thick and 8,000-kg-m^{-3}-dense inner core. Our results indicate a scenario that might require a complement of light elements dissolved in the iron inner core[21,22].

In a preliminary conclusion, using only geophysical observations and without imposing any constraints on the chemical compositions of the layers, the structure including both a viscous outer core and a solid inner core does not show a statistical advantage over a structure without an inner core. Both cases are acceptable. Other considerations have to be invoked. For the low viscosity zone (LVZ), we note three important results. First, we confirm the existence of a LVZ at the CMB for both lunar models, with or without an inner core. The size and the viscosity of the LVZ are compatible with those previously proposed[14]. For a Moon with or without a solid core, the density found for the LVZ is more than 3,465 kg m^{-3} (3,884 ± 300 kg m^{-3} without an inner core and 3,559 ± 94 kg m^{-3} with an inner core). This range of density is larger than the lunar mantle density profile derived from ref. 3 ($\rho_m \approx 3{,}300$ kg m^{-3}) but is in the range of IBCs densities at the LVZ temperature and pressure ($\rho_{IBC} > 3{,}450$ kg m^{-3})[23,24]. We remind that the presence of IBCs at the CMB is the main marker of the DLMO scenario[6,11]. Second, the density jump between the LVZ and the mantle, leading to average density ratios of about 1.06 and 1.15 for a Moon model with and without a solid inner core, respectively, is consistent with that expected with a DLMO[6]. Third, in the context of a DLMO event, it is expected that the viscosity jump between the mantle and the LVZ is at least about one order of magnitude[11]. In our results, only the set of models including a solid inner core proposes such a contrast—with 10^{21} Pa s for the mantle versus about 10^{18} Pa s for the LVZ on average—whereas without an inner core, the contrast between the mantle viscosity (10^{21} Pa s) and that of the LVZ (about 10^{17} Pa s) is more important.

Thermodynamical constraints

On the basis of the structures presented in Table 1, we computed the temperature ratio between the top of the LVZ (mantle temperature) and the bottom of the LVZ (core temperature), considering a wide range of possible viscosities, enthalpies and, consequently, chemical compositions for the LVZ (see Methods for details and the hypothesis used to estimate the LVZ temperature). We considered chemical compositions based on two main titanium oxide proportions: ilmenite-free and ilmenite-rich. Ilmenite-free is represented by the dunite (100% dry olivine and 0% titanium oxide) of ref. 25 and the lherzolite (Earth-like mantle material composed of olivine + clinopyroxene + orthopyroxene + garnet with 0% titanium oxide) of ref. 26. Ilmenite-rich is characterized by lherzolite-bearing ilmenite (olivine +clinopyroxene + orthopyroxene + 8% ilmenite, corresponding to the bulk composition of ref. 24) and the 100% ilmenite cumulate (ranging from pure ilmenite100 ($FeTiO_3$) to ilmenite40 ($Fe_{0.4}Mg_{0.6}(TiO_3)$)) following the analysis of ref. 13 (see Methods for details on the chemical composition of the LVZ). The choice for these assemblages is driven by the published values of the corresponding activation enthalpies (refs. 13,24–26).

We perform thermodynamic simulations (see Methods), using the Perple_X program[27], to compute the temperature of the LVZ (T_{LVZ}) from the four considered chemical compositions and the 2σ interval of our estimated mantle and LVZ viscosities (Table 1). The derived range of temperatures is plotted as a function of density (ρ_{LVZ}) and activation enthalpy (H^*) and is shown by the grey areas in Fig. 1, for models without (Fig. 1a,b) and with (Fig. 1c,d) an inner core. In the case of models with an inner core (Fig. 1c,d), there are areas in which thermodynamic simulations (T_{LVZ}, ρ_{LVZ}) intercept the geophysical constraints interval (T_{LVZ}, H^*), as highlighted by the light-red area. This is clearly the case for the ilmenite-rich assemblages. On the contrary, models for the ilmenite-free (that is, the dunite and the lherzolite) cumulates do not show any overlap between thermodynamic profiles and geophysical intervals. This is also visible in Extended Data Table 1, in which the cases of possible overlaps between Perple_X density intervals and geophysical ones are indicated. Models without an inner core do not show overlaps between the thermodynamic profiles and the geophysical interval for both ilmenite-free and ilmenite-rich assemblages (Fig. 1a,b).

These results show that only ilmenite-rich thermodynamic profiles with inner core match the density, temperature and viscosity deduced from observations of the lunar tidal deformations. So, without an inner core, the LVZ densities obtained from geophysical constraints are not compatible with the expected thermodynamic density profiles deduced from Perple_X for the most likely mineral assemblages adopted for this layer. The same conclusions can be drawn from Extended Data Table 1, in which we can see that only models with an inner core and with a LVZ containing ilmenite have intervals of densities simulated with Perple_X for the range of temperatures proposed by the geophysical constraints, compatible with the geophysical densities. For the models without an inner core, the comparisons between the tidal constraints and the thermodynamic simulations are all incompatible.

A Moon with an inner core and a global overturned mantle

From this work, two main results can be discussed. First, we confirm the existence of a LVZ gathering, all the requirements of an ilmenite-rich layer. Second, together with this ilmenite-rich LVZ, to reconcile temperature gradient at the CMB, thermodynamic profiles and geophysical constraints, only a Moon with a viscous outer core and a solid inner core is possible. These two conclusions, by their simultaneity, enhance the scenario of a DLMO in the context of a differentiated Moon interior with a solid inner core. The consequences of such a structure are important. First, considering the global chronology of the Solar System evolution, ref. 8 demonstrated that a DLMO may explain the HSE content of

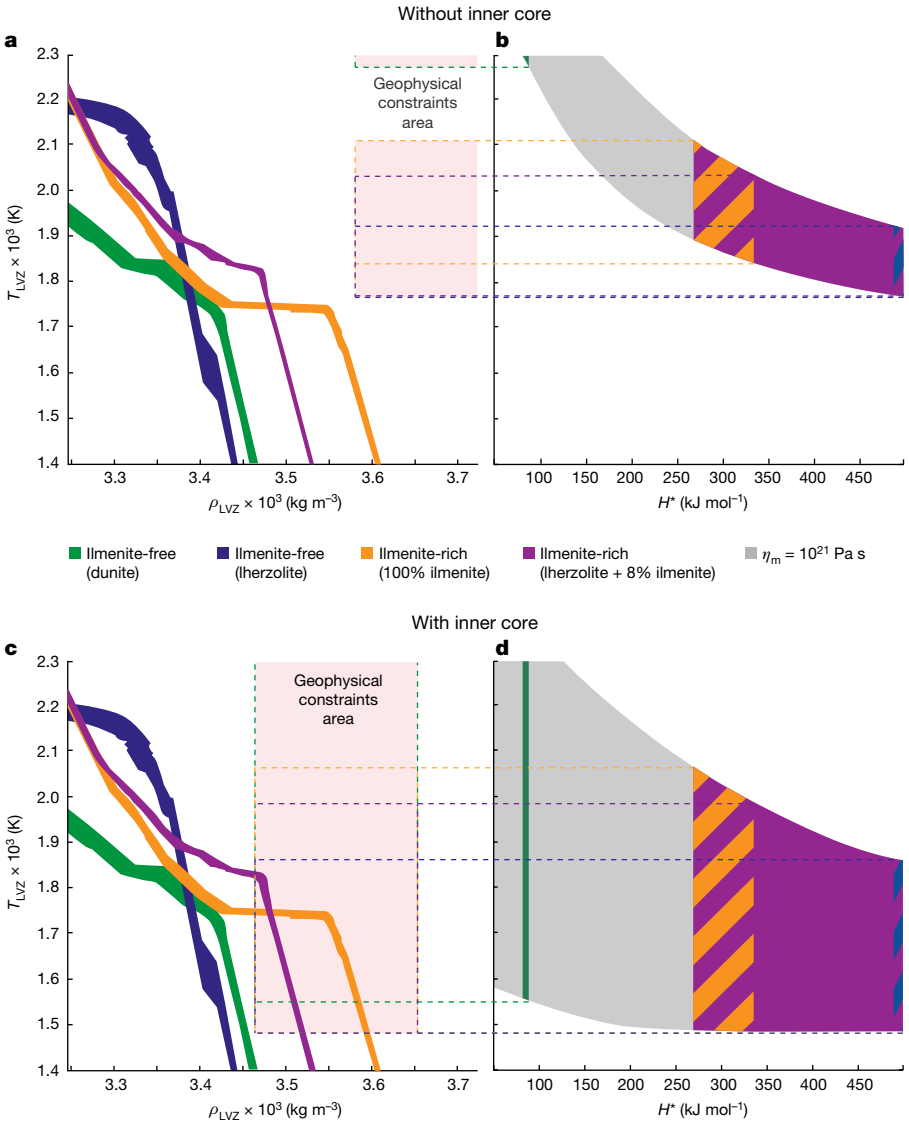

Fig. 1 | Moon temperature and density profiles. a,**c**, LVZ temperature (T_{LVZ}) as a function of LVZ density (ρ_{LVZ}) deduced from the thermodynamic models at the LVZ pressure spanning from 4.2 to 4.6 GPa. **b**,**d**, LVZ temperature (T_{LVZ}) deduced from geophysical constraints as a function of the activation enthalpy H^*. **a** and **b** correspond to models without an inner core, whereas **c** and **d** correspond to models with an inner core. Grey zones in **b** and **d** are derived from the geophysical constraints, whereas light-red zones are the overlapping areas between the geophysical and thermodynamic models. η_m, mantle viscosity.

the lunar mantle and favours the accretion tail hypothesis against the Late Heavy Bombardment that affected the Moon about 3.9 Gyr ago. The Late Heavy Bombardment would indeed have delivered about ten times the mass constrained by the HSEs abundances in the lunar mantle than the accretion tail scenario. This scenario is also consistent with the chronology of the outer planet orbital evolution, as the accretion tail scenario does not require that the instability of the giant planets occurred a long time after the removal of the protoplanetary disk[8,28]. Second, the existence of a solid inner core is crucial for understanding the mechanism leading to the appearance or not of a planetary magnetic field. For instance, the growing of an Earth inner core participates in outer core convection. Therefore, its nucleation is believed to have driven a strong increase in the power available to the dynamo[29]. Magnetic studies of lunar rocks reported that, between 4.25 and 3.56 Gyr ago, the Moon had a strong core dynamo (with surface field intensities of approximately 20–10 μT) that subsequently declined 3.19 Gyr ago (to <4 μT)[30]. The confirmation of the existence of a Moon solid inner core is therefore a key factor for understanding the evolution of its magnetic field. Finally, a way to strengthen our results could be to increase the number of different assemblages for which activation enthalpies are accurately measured by laboratory experiments at lunar CMB pressure and temperature conditions.

Online content

Any methods, additional references, Nature Portfolio reporting summaries, source data, extended data, supplementary information, acknowledgements, peer review information; details of author contributions and competing interests; and statements of data and code availability are available at https://doi.org/10.1038/s41586-023-05935-7.

1. Nakamura, Y. et al. in *Encyclopedia of Planetary Science. Encyclopedia of Earth Science* Vol. 10, 2299–2309 (Springer, 1979).
2. Weber, R. C., Lin, P.-Y., Garnero, E. J., Williams, Q. & Lognonné, P. Seismic detection of the lunar core. *Science* **331**, 309–312 (2011).
3. Garcia, R. F. et al. Lunar seismology: an update on interior structure models. *Space Sci. Rev.* **215**, 50 (2019).
4. Snyder, G. A. et al. in *Workshop on Geology of the Apollo 17 Landing Site* (eds Ryder, G., Schmitt, H. H. & Spudis, P. D.) 53–55 (Lunar and Planetary Institute, 1992).

5. Elphic, R. C. et al. Lunar Fe and Ti abundances: comparison of Lunar Prospector and Clementine data. *Science* **281**, 1493–1496 (1998).
6. Li, H. et al. Lunar cumulate mantle overturn: a model constrained by ilmenite rheology. *J. Geophys. Res. Planets* **124**, 1357–1378 (2019).
7. Wieczorek, M. A. in *Treatise on Geophysics: Planets and Moons* Vol. 10 (ed. Schubert, G.) 165–206 (Elsevier, 2007).
8. Morbidelli, A. et al. The timeline of the lunar bombardment: revisited. *Icarus* **305**, 262–276 (2018).
9. Hess, P. C. & Parmentier, E. A model for the thermal and chemical evolution of the Moon's interior: implications for the onset of mare volcanism. *Earth Planet. Sci. Lett.* **134**, 501–514 (1995).
10. Zhong, S., Parmentier, E. & Zuber, M. T. A dynamic origin for the global asymmetry of lunar mare basalts. *Earth Planet. Sci. Lett.* **177**, 131–140 (2000).
11. Zhang, N., Dygert, N., Liang, Y. & Parmentier, E. The effect of ilmenite viscosity on the dynamics and evolution of an overturned lunar cumulate mantle. *Geophys. Res. Lett.* **44**, 6543–6552 (2017).
12. Dygert, N., Hirth, G. & Liang, Y. A flow law for ilmenite in dislocation creep: implications for lunar cumulate mantle overturn. *Geophys. Res. Lett.* **43**, 532–540 (2016).
13. Tokle, L., Hirth, G., Liang, Y., Raterron, P. & Dygert, N. The effect of pressure and Mg-content on ilmenite rheology: implications for lunar cumulate mantle overturn. *J. Geophys. Res. Planets* **126**, e2020JE006494 (2021).
14. Tan, Y. & Harada, Y. Tidal constraints on the low-viscosity zone of the Moon. *Icarus* **365**, 114361 (2021).
15. Melini, D., Saliby, C. & Spada, G. On computing viscoelastic Love numbers for general planetary models: the ALMA^3 code. *Geophys. J. Int.* **231**, 1502–1517 (2022).
16. Briaud, A. et al. Constraints on the lunar core viscosity from tidal deformation. *Icarus* **394**, 115426 (2023).
17. Wieczorek, M. A. et al. The crust of the Moon as seen by GRAIL. *Science* **339**, 671–675 (2013).
18. Morard, G. et al. Liquid properties in the Fe-FeS system under moderate pressure: tool box to model small planetary cores. *Am. Mineral.* **103**, 1770–1779 (2018).
19. Harada, Y. et al. The deep lunar interior with a low-viscosity zone: revised constraints from recent geodetic parameters on the tidal response of the Moon. *Icarus* **276**, 96–101 (2016).
20. Viswanathan, V., Rambaux, N., Fienga, A., Laskar, J. & Gastineau, M. Observational constraint on the radius and oblateness of the lunar core-mantle boundary. *Geophys. Res. Lett.* **46**, 7295–7303 (2019).
21. Stähler, S. C. et al. Seismic detection of the martian core. *Science* **373**, 443–448 (2021).
22. Murphy, C. A. in *Deep Earth: Physics and Chemistry of the Lower Mantle and Core* (eds Terasaki, H. & Fischer, R. A.) 253–264 (Wiley, 2016).
23. Matsumoto, K. et al. Internal structure of the Moon inferred from Apollo seismic data and selenodetic data from GRAIL and LLR. *Geophys. Res. Lett.* **42**, 7351–7358 (2015).
24. Mallik, A., Ejaz, T., Shcheka, S. & Garapic, G. A petrologic study on the effect of mantle overturn: implications for evolution of the lunar interior. *Geochim. Cosmochim. Acta* **250**, 238–250 (2019).
25. Karato, S.-I. & Wang, D. in *Physics and Chemistry of the Deep Earth* (ed. Karato, S.-I.) 145–182 (Wiley, 2013).
26. Karato, S.-i Rheology of the deep upper mantle and its implications for the preservation of the continental roots: a review. *Tectonophysics* **481**, 82–98 (2010).
27. Connolly, J. Multivariable phase diagrams; an algorithm based on generalized thermodynamics. *Am. J. Sci.* **290**, 666–718 (1990).
28. Gomes, R., Levison, H. F., Tsiganis, K. & Morbidelli, A. Origin of the cataclysmic Late Heavy Bombardment period of the terrestrial planets. *Nature* **435**, 466–469 (2005).
29. Landeau, M., Fournier, A., Nataf, H.-C., Cébron, D. & Schaeffer, N. Sustaining Earth's magnetic dynamo. *Nat. Rev. Earth Environ.* **3**, 255–269 (2022).
30. Suavet, C. et al. Persistence and origin of the lunar core dynamo. *Proc. Natl Acad. Sci. USA* **110**, 8453–8458 (2013).

Methods

Geophysical constraints on Moon inner structure

Model of tidal deformations. The Moon has a measurement of the degree 2 radial motion of its deformation (h_2) obtained from laser altimetry (for example, refs. 31–33) and lunar laser ranging (LLR)[20,34]. Associated with this deformation of the Moon, the degree 2 gravity potential change (k_2) is well constrained with the GRAIL mission[35]. The GRAIL mission also gives an estimate of the mass and the moment of inertia of the Moon, which imposes two further important constraints for its inner structure[34]. Moreover, almost 50 years of accurate LLR measurements constrain the tidal lunar dissipation, providing quality factors (Q) at monthly and yearly periods[3,34]. Also, seismic profiles give a good overview of the structure of the mantle but poor constraints on the physical properties (rigidity, density, viscosity) of the boundary between the mantle and the core and the deep inner structure of the core. Hence, non-unique solutions for the interpretation of the seismic profiles are given with and without an inner core[2,3,14]. To set our lunar models, we consider two types of inner structure following the previous studies of refs. 2,3,36,37. For the core, we choose the two end-members models from refs. 2,3. These models differ in their core structures. These studies have indeed reported divergences in S-wave and P-wave velocities owing to high attenuation below 1,200 km depth. As a consequence, it is difficult to interpret the structure below this limit. According to ref. 20, the Moon is solely composed of a unique fluid core, with a radius of 381 ± 12 km. In ref. 2, a two-layer core is proposed with a radius of 330 km composed by a 90-km-thick fluid outer core and a 240-km-thick solid inner core. Other analysis of the tidal dissipation and the Love numbers found evidence of a much less rigid deep region at the CMB than the mantle[3,38]. Furthermore, the LVZ has been stated to be partially molten with a low viscosity to explain the quality factor[37]. For the mantle, we adopt viscosity and rigidity profiles similar to ref. 37, assuming a linear stress–strain relationship (that is, Maxwell rheology; Extended Data Table 3). For the crust, the thickness is about 38.5 km, corresponding to the GRAIL average crustal model with a density depending on the average crustal porosity[39]. Throughout our models, we kept the same values for the mantle and the crust parameters. Hence, for our models, we adopt two types of lunar inner structure: (1) with a crust, a mantle, a viscous core and a LVZ at the interface between the mantle and the core, and (2) with a more complex core structure assuming an elastic inner core (with infinite viscosity) surrounded by a viscous outer core. Extended Data Table 2 presents the values, along with their uncertainties and references, of the mean radius (R) of the Moon, the mass (M), the normalized moment of inertia (C/MR^2), the tidal Love numbers of degree 2 (h_2 and k_2) and the monthly and yearly quality factors (Q_f, $Q_{f'}$) used for selecting our Moon models. The mass and moment of inertia are derived from the GRAIL degree 2 gravity coefficients[3,34]. We use the estimations of quality factors for the same two frequencies as estimated by ref. 3. To constrain the Love number k_2, we use the value obtained from the analysis of the GRAIL data[34]. This value is indeed better constrained by one order of magnitude of the estimated uncertainties in comparison with the LLR determination. Furthermore, the tidal Love number h_2 is also considered. However, because of the large differences reported in refs. 40,41, we use the range between their two possible intervals to constrain our models.

To operate the random-walk Monte Carlo, we sample using a uniform distribution the radius, densities and viscosities for each layer of the Moon interior. The intervals of the uniform exploration are given in Extended Data Table 3. For each of the 120,000 Moon models, we calculate the total mass and the moment of inertia, as well as the real and imaginary parts of the tidal Love numbers. These are estimated using the ALMA code[16,42]. We also deduce the quality factors. At the end of the process, we select 0.12% of models including k_2, h_2, monthly and yearly quality factors, mass and the moment of inertia, consistent with the published values (see Extended Data Table 2 and Extended Data Fig. 1). Extended Data Fig. 1 shows the histograms of the relative difference between observational constraints (that is, mass, moment of inertia, tidal Love numbers and quality factors) given in Extended Data Table 2 and their values obtained from the selected models. The constraints on the mass is very small. This is expected, as we introduce a compensation mechanism for keeping the mass close to the observation value, despite the variation of densities and radius of the layers. Extended Data Figs. 2 and 3 show the distribution of the radius, thickness density and viscosity of the lunar inner layers obtained after filtering for the mass, moment of inertia, Love numbers and quality factors. The average as well as the 2σ uncertainty are given in Extended Data Table 2.

Sensitivity to the mantle viscosity. The results presented in the previous section were obtained by fixing the Moon mantle viscosity to 10^{21} Pa s. This value is appropriate for the dry peridotite given the lunar mantle temperature and pressure profile[14,43]. However, depending on the water content, the mantle viscosity could be lower[6,44]. Despite that, we also simulated stronger lunar mantle viscosity (that is, $>10^{21}$ Pa s) with the ALMA code to test how the tidal Love numbers and the quality factor behave with regards to an unrealistic viscosity at mantle temperature–pressure conditions. First, we estimate the variations in k_2 and the monthly quality factor Q in considering different values of viscosities from 10^{18} to 10^{24} Pa s. As can be seen in Extended Data Fig. 4, when considering the ratio between k_2 and Q, only the results with viscosities greater than 10^{20} Pa s match the observational constraints indicated by the dots and the error bars. On the basis of this first conclusion, we proceed with the method described previously (see previous section) for computing temperature profiles at the LVZ and for comparing the interval of possible densities as derived from geophysical constraints with that deduced from thermochemical modelling (Perple_X). As shown in Extended Data Fig. 5, the conclusions remain the same: for the models including an inner core together with an ilmenite-rich LVZ, there is a good match between the density profiles obtained with the thermodynamic modelling (Extended Data Fig. 5d) and the interval of densities deduced from our deformation model (Extended Data Fig. 5c), whereas for the models without an inner core and/or with ilmenite-free LVZ, there is no possible match (see Extended Data Fig. 5a,b).

Sensitivity of the filtering criteria to the internal structure parameterization. To evaluate which parameters of the Moon profile (rigidity, viscosity, radius and density) affect the deformation the most, the total mass and moment of inertia simulations have been performed considering variations in the values of the parameters presented in Extended Data Table 3 for a given arbitrary model. With these modified inputs, we estimated the deformation variables (tidal Love numbers and quality factors) as well as the Moon total mass and moment of inertia. Extended Data Fig. 6 plots the ratio between the differences for these estimated quantities and the initial values. As can be seen, the total mass and moment of inertia are mainly sensitive to mantle radius but also to the radii of the other layers as well as their densities. The Love numbers are mainly driven by the rigidities and radii of the mantle and LVZ as well as the outer core viscosity. Oppositely, the quality factors are more sensitive to the characteristics of the deepest layers, the outer core and inner core radii, the outer core viscosity and the LVZ rigidity.

LVZ characteristics and thermal state

LVZ composition. The LVZ region is stated to be partially molten with a gradient in viscosity and density with respect to the overlying mantle. The DLMO has been proposed to explain the concentration of HSEs provided by the geochemical and petrological analyses of lunar rocks[39,45,46]. The lunar rocks are known for their higher contents of TiO_2 and FeO than the Earth (that is, more than 8%), for example, refs. 12,24,45. This Ti content of lunar basalts is believed to be related to the late stage

of magma ocean cumulates that were enriched in ilmenite[36]. To explain the high content in HSE, the DLMO has been proposed to explain the asymmetrical concentration of incompatible trace elements in the KREEP region[6]. It is thought that the DLMO is the consequence of the lunar magma ocean crystallization. The solidification of the lunar magma ocean starts as follows: olivine orthopyroxene, anorthitic feldspars and then clinopyroxene. The ilmenite becomes thus a liquid Fe-rich phase together with anorthite and clinopyroxene near the lunar magma ocean solidification (that is, 95% of lunar magma ocean crystallization)[6,9,12,47]. After reaching the ilmenite saturation, the late cumulates that consist mainly of ilmenite, clinopyroxene and KREEP components are thus denser than the underlying early mafic cumulates (composed mainly by magnesium olivine and orthopyroxene). The resulting unstable density stratification beneath the anorthitic crust may have caused the solid-state cumulate to overturn[9,12]. These underplated dense cumulates may have sunk into the lunar mantle as they crystallized, forming thick IBCs, with a long-term steady state owing to its neutral buoyancy at the CMB[6,9,12,13,24,48]. The overturn event would require some portions of both the Fe-rich IBCs layer and the underlying magnesium-rich mantle to balance each other, producing compositional variations in both layers with time[6,9,12,13,24,48]. From the reanalysis of the ilmenite samples, the LVZ probably contains 3–9 wt% ilmenite with composition between ilmenite100 ($FeTiO_3$) and ilmenite40 ($Fe_{0.4}Mg_{0.6}(TiO_3)$), at pressures ranging from 1 to 5 GPa from the reanalysis of ilmenite samples from refs. 12,13. Moreover, the proposed range of Fe-Mg content has been chosen because it is in a chemical equilibrium with the mafic mantle at the mantle temperatures ranging between 1,300 and 1,500 K (refs. 13,49). Finally, the range of activation enthalpies that we use for this work agrees with the estimation of ref. 50.

Thermal equations. We estimate the temperature ratio between the mantle–LVZ interface and the LVZ–core interface $\Delta T_{LVZ}/T_m$ as a function of the ratio η_m/η_{LVZ} as proposed by ref. 26:

$$\frac{\Delta T_{LVZ}}{T_m} = \frac{ln\left(\frac{\eta_m}{\eta_{LVZ}}\right)}{\frac{H^*}{RT_m} - ln\left(\frac{\eta_m}{\eta_{LVZ}}\right)}$$

for which the temperature at the LVZ–core interface, is a function of three variables, that is, the temperature of the mantle–LVZ interface (T_m), the ratio of the mantle (η_m) and the LVZ (η_{LVZ}) viscosities and the activation enthalpy (H^*). The η_m/η_{LVZ} ratio is estimated from our results for each selected model. The temperature at the mantle–LVZ interface is defined according to ref. 36 at the given depth (z_m; see Extended Data Table 4). Reference 36 showed marginal posterior probability density function profiles of the Moon depicting the modelled temperature as a function of depth. They have fixed depth node histograms, reflecting the probability density function of the sampled temperatures. By lining up these marginals, the temperature can be thought of as contours directly related to probability occurrence. The range of allowed LVZ temperatures is listed in Extended Data Table 4.

Thermodynamical simulations. From the Gibbs energy minimization model, we calculated temperature versus density profiles of four possible chemical compositions inferred from four mineralogical assemblages: dunite (100% dry olivine), lherzolite (Earth-like mantle with olivine + clinopyroxene + orthopyroxene + garnet), 100% ilmenite (only ilmenite with composition between ilmenite100 ($FeTiO_3$) and ilmenite40 ($Fe_{0.4}Mg_{0.6}(TiO_3)$)) and lherzolite with 8 wt% ilmenite at LVZ pressure (from 4.3 to 4.6 GPa). We performed this calculation using Perple_X program[27] with the thermodynamic database of ref. 51. It considers the mineral-phase transformations computed with the equation of state of ref. 52. For the mineral solid solutions used in the models, we used the dataset of ref. 53 for the olivine, clinopyroxene, orthopyroxene and garnet and the dataset of ref. 54 for the ilmenite. To quantify the partial melting, we considered the thermodynamical model in the system KNCFMASHTOCr from ref. 55.

Data availability

The dataset used in this study is provided at https://doi.org/10.5281/zenodo.7661158.

Code availability

The code ALMA3 is freely available at https://github.com/danielemelini/ALMA3. The code Perple_X is freely available at https://www.perplex.ethz.ch.

31. Mazarico, E., Barker, M. K., Neumann, G. A., Zuber, M. T. & Smith, D. E. Detection of the lunar body tide by the Lunar Orbiter Laser Altimeter. *Geophys. Res. Lett.* **41**, 2282–2288 (2014).
32. Steinbrügge, G. et al. Viscoelastic tides of Mercury and the determination of its inner core size. *J. Geophys. Res. Planets* **123**, 2760–2772 (2018).
33. Bürgmann, R., Rosen, P. A. & Fielding, E. J. Synthetic aperture radar interferometry to measure Earth's surface topography and its deformation. *Annu. Rev. Earth Planet. Sci.* **28**, 169–209 (2000).
34. Williams, J. G. et al. Lunar interior properties from the GRAIL mission. *J. Geophys. Res. Planets* **119**, 1546–1578 (2014).
35. Williams, J. G. & Boggs, D. H. Tides on the Moon: theory and determination of dissipation. *J. Geophys. Res. Planets* **120**, 689–724 (2015).
36. Khan, A., Connolly, J. A., Pommier, A. & Noir, J. Geophysical evidence for melt in the deep lunar interior and implications for lunar evolution. *J. Geophys. Res. Planets* **119**, 2197–2221 (2014).
37. Harada, Y. et al. Strong tidal heating in an ultralow-viscosity zone at the core–mantle boundary of the Moon. *Nat. Geosci.* **7**, 569–572 (2014).
38. Khan, A., Mosegaard, K., Williams, J. & Lognonné, P. Does the Moon possess a molten core? Probing the deep lunar interior using results from LLR and Lunar Prospector. *J. Geophys. Res. Planets* **109**, E09007 (2004).
39. Wieczorek, M. A. et al. The constitution and structure of the lunar interior. *Rev. Mineral. Geochem.* **60**, 221–364 (2006).
40. Viswanathan, V., Fienga, A., Gastineau, M. & Laskar, J. INPOP17a planetary ephemerides. Notes Scientifiques et Techniques de l'Institut de mécanique séleste, #108 (2017).
41. Thor, R. N. et al. Determination of the lunar body tide from global laser altimetry data. *J. Geod.* **95**, 4 (2021).
42. Spada, G. ALMA, a Fortran program for computing the viscoelastic Love numbers of a spherically symmetric planet. *Comput. Geosci.* **34**, 667–687 (2008).
43. Karato, S.-I. Geophysical constraints on the water content of the lunar mantle and its implications for the origin of the Moon. *Earth Planet. Sci. Lett.* **384**, 144–153 (2013).
44. Karato, S.-I. & Wu, P. Rheology of the upper mantle: a synthesis. *Science* **260**, 771–778 (1993).
45. Delano, J. W. Pristine lunar glasses: criteria, data, and implications. *J. Geophys. Res. Solid Earth* **91**, 201–213 (1986).
46. Zhao, Y., De Vries, J., van den Berg, A., Jacobs, M. & van Westrenen, W. The participation of ilmenite-bearing cumulates in lunar mantle overturn. *Earth Planet. Sci. Lett.* **511**, 1–11 (2019).
47. Wyatt, B. The melting and crystallisation behaviour of a natural clinopyroxene-ilmenite intergrowth. *Contrib. Mineral. Petrol.* **61**, 1–9 (1977).
48. van Kan Parker, M. et al. Neutral buoyancy of titanium-rich melts in the deep lunar interior. *Nat. Geosci.* **5**, 186–189 (2012).
49. Andersen, D. J. & Lindsley, D. H. in *Tenth Lunar and Planetary Science Conference* 493–507 (Pergamon, 1980).
50. Yu, S. et al. Overturn of ilmenite-bearing cumulates in a rheologically weak lunar mantle. *J. Geophys. Res. Planets* **124**, 418–436 (2019).
51. Holland, T. & Powell, R. An improved and extended internally consistent thermodynamic dataset for phases of petrological interest, involving a new equation of state for solids. *J. Metamorph. Geol.* **29**, 333–383 (2011).
52. Holland, T. & Powell, R. An internally consistent thermodynamic data set for phases of petrological interest. *J. Metamorph. Geol.* **16**, 309–343 (1998).
53. Xu, W., Lithgow-Bertelloni, C., Stixrude, L. & Ritsema, J. The effect of bulk composition and temperature on mantle seismic structure. *Earth Planet. Sci. Lett.* **275**, 70–79 (2008).
54. Andersen, D. J. & Lindsley, D. H. Internally consistent solution models for Fe-Mg-Mn-Ti oxides; Fe-Ti oxides. *Am. Mineral.* **73**, 714–726 (1988).
55. Holland, T. J., Green, E. C. & Powell, R. Melting of peridotites through to granites: a simple thermodynamic model in the system KNCFMASHTOCr. *J. Petrol.* **59**, 881–900 (2018).

Acknowledgements We thank A. Morbidelli and M. Wieczorek for their careful reading of the manuscript and H. Hussman, A. Stark, G. Spada, D. Melini, V. Viswanathan and D. Andrault for their fruitful discussions. We would like to thank K. Mosegaard and an anonymous reviewer for their constructive reviews that improved the paper. This project has been supported by the French ANR, project LDLR (Lunar tidal Deformation from earth-based and orbital Laser Ranging) number ANR-19-CE31-0026, and the European Research Council (ERC) under the European Union's Horizon 2020 research and innovation programme (Advanced Grant AstroGeo-885250).

Author contributions A.B. and A.F. conceived the preliminary idea and C.G., A.M. and N.R. participated in its development. A.B. performed the computations and made most of the plots. A.B. and C.G. set up the petrochemical assumptions and designed the thermodynamical simulations. A.B., C.G. and A.F. wrote the text. A.F. and C.G. contributed to the design of the figures. A.M. and N.R. contributed to the final version of the manuscript.

Competing interests The authors declare no competing interests.

Additional information

Supplementary information The online version contains supplementary material available at https://doi.org/10.1038/s41586-023-05935-7.

Correspondence and requests for materials should be addressed to Arthur Briaud or Agnès Fienga.

Peer review information *Nature* thanks Klaus Mosegaard and the other, anonymous, reviewer(s) for their contribution to the peer review of this work. Peer reviewer reports are available.

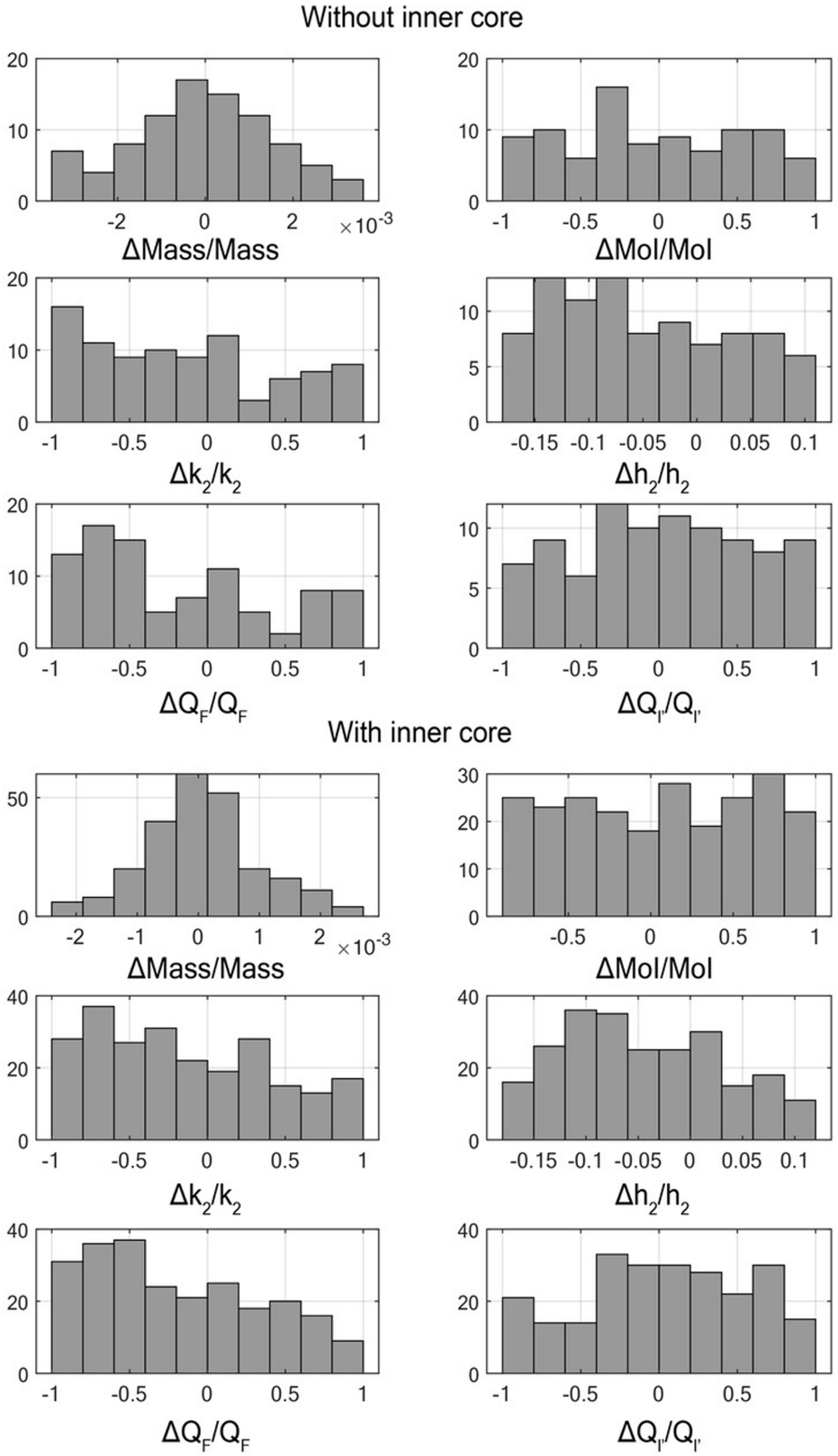

Extended Data Fig. 1 | Histograms of relative differences between observables and models. Histograms of relative differences over their 3σ uncertainties between the values of the observational constraints given in Extended Data Table 2 and the values of the same parameters but extracted from our models for models without an inner core (top) and with an inner core (bottom).

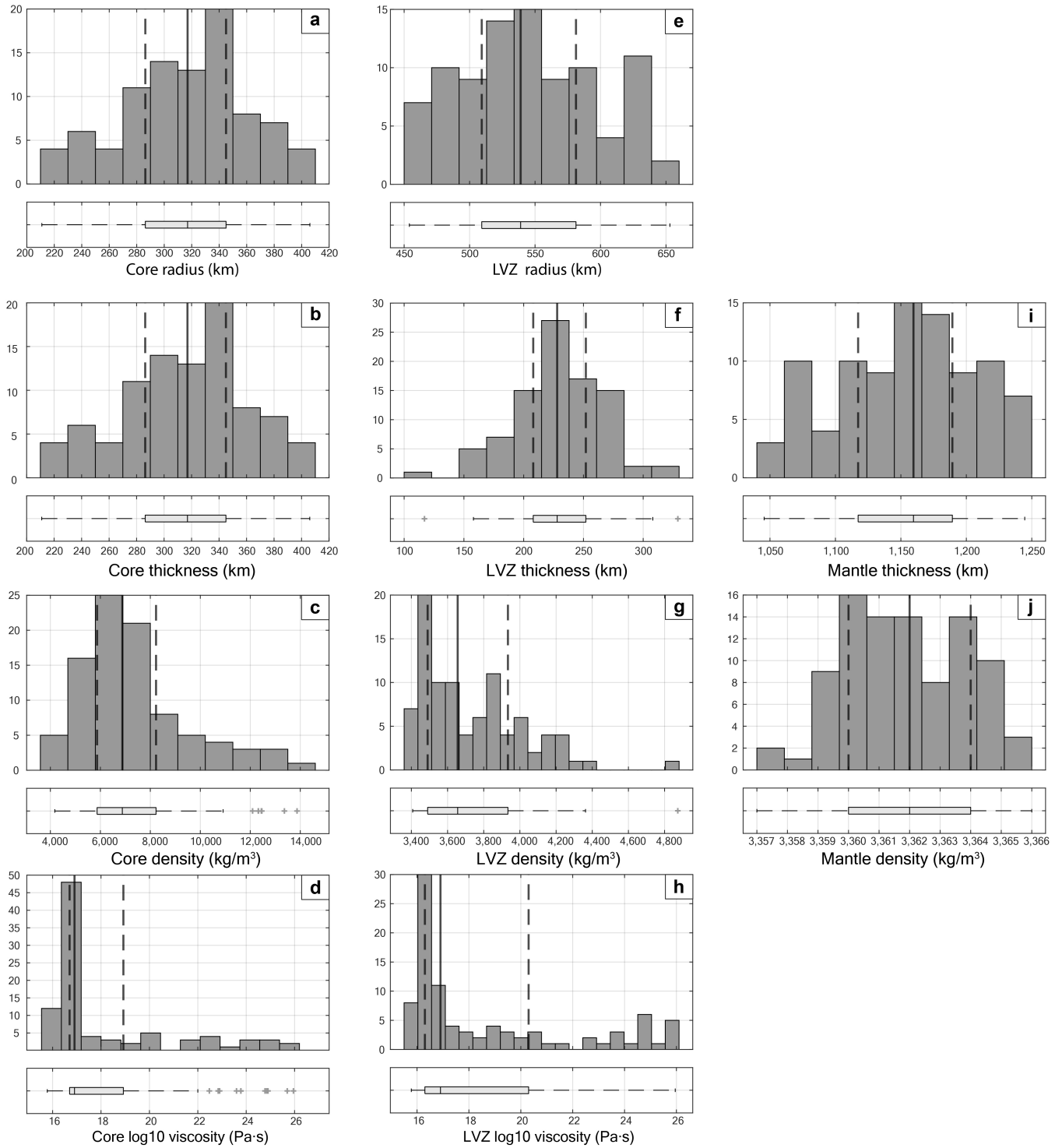

Extended Data Fig. 2 | Model without inner core distribution after filtering the geodetic parameters. a–**d**, Distribution of the core parameters. Distributions of the LVZ (**e**–**h**) and the mantle (**i**,**j**). Black and dashed grey lines correspond to the median and the 25th and 75th percentiles, respectively.

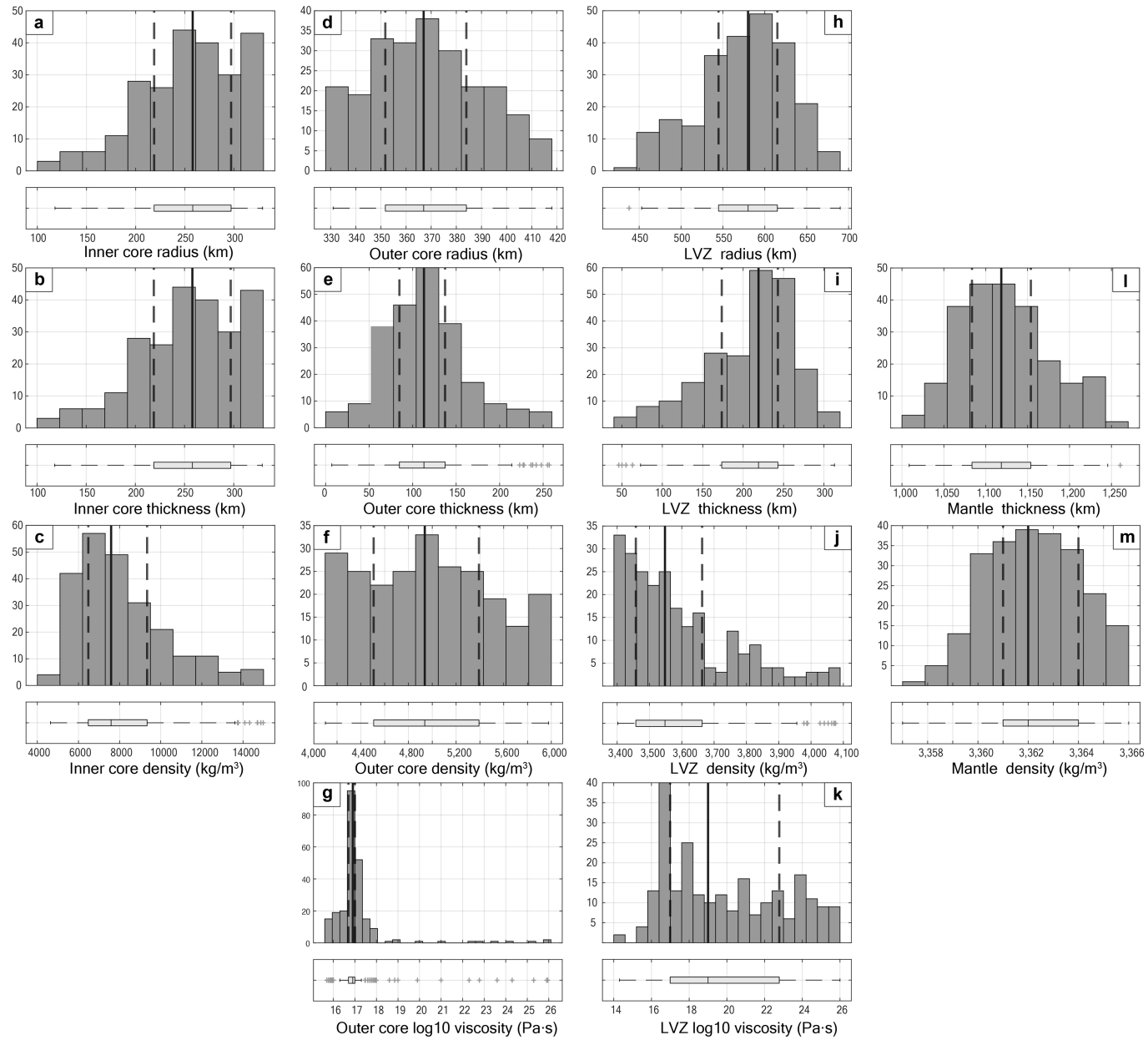

Extended Data Fig. 3 | Model with inner core distribution after filtering the geodetic parameters. a–**c**, Distribution of the inner core parameters. Distributions of the outer core (**d**–**g**), the LVZ (**h**–**k**) and the mantle (**l**,**m**). Black and dashed grey lines correspond to the median and the 25th and 75th percentiles, respectively.

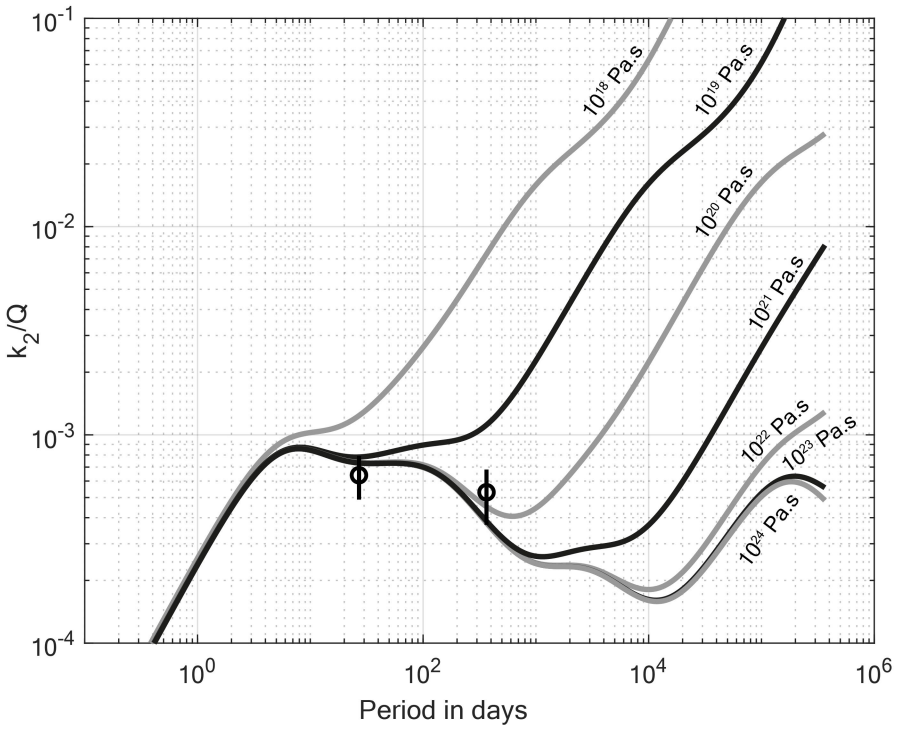

Extended Data Fig. 4 | Behaviour of the k_2 and Q ratio over the tidal periods. The Delaunay arguments F and ℓ′ correspond to periods defined in ref. 35 of 27.212 days and 365.260 days, respectively. Error bars refer to 1σ.

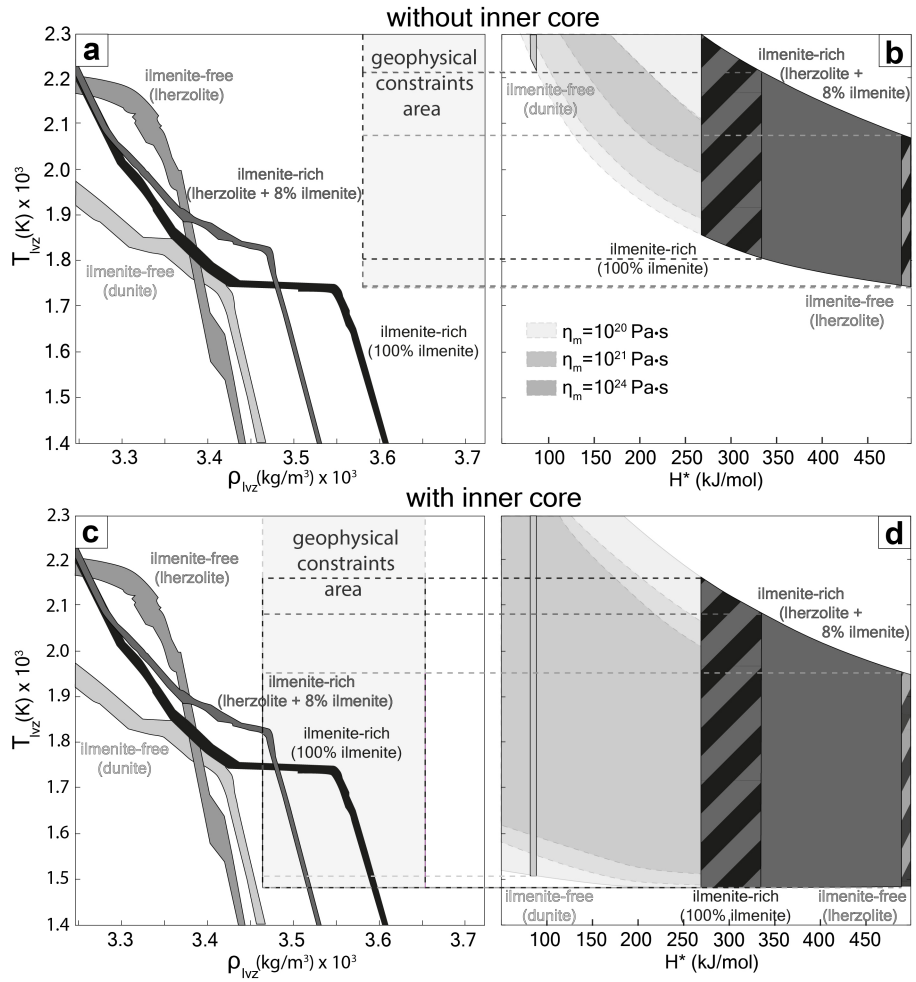

Extended Data Fig. 5 | Temperature and density profiles for different mantle viscosities. a,**c**, LVZ temperature (T_{LVZ}) as a function of LVZ density (ρ_{LVZ}) deduced from the thermodynamic models at the LVZ pressure spanning from 4.2 to 4.6 GPa. **b**,**d**, LVZ temperature (T_{LVZ}) as a function of the activation enthalpy (H^*). For more details, see Fig. 1. Grey areas correspond to mantle viscosities (η_m) that are in agreement with the geophysical constraints.

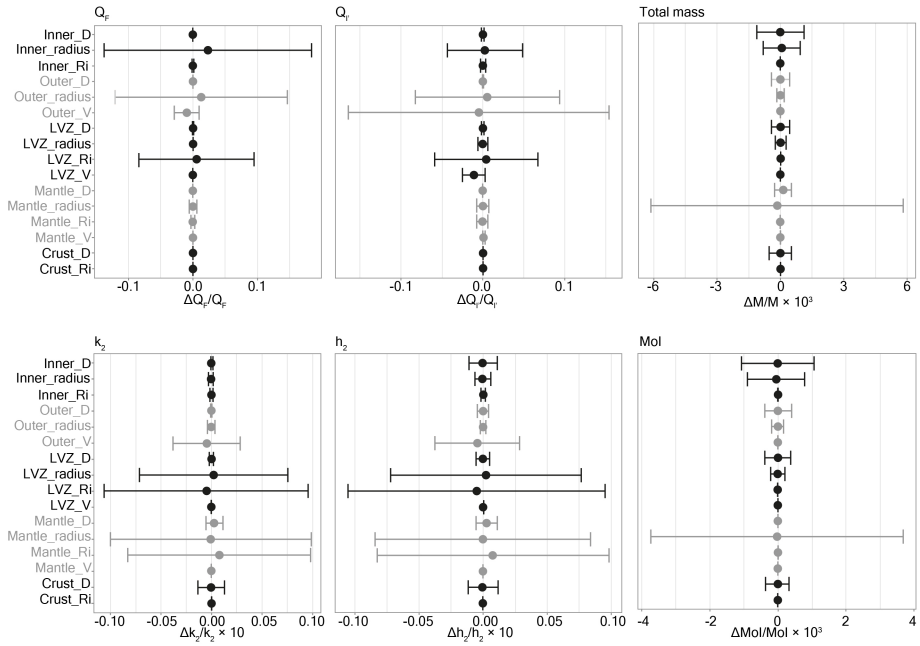

Extended Data Fig. 6 | Sensitivity analysis of geodetic parameters to the lunar interior characteristics. Sensitivity of the mass, moment of inertia, tidal Love numbers and quality factors Q_{ℓ}, and Q_F to the input parameters: radius, viscosity V, rigidity Ri and density D for each layer (crust C, mantle M, low-velocity zone L, outer core OC and inner core IC). Variations are about 10% around the model reference values.

Extended Data Table 1 | Intervals of LVZ densities inferred by tidal deformation and thermodynamical models

	Ilmenite-free Dunite	Ilmenite-free Lherzolite	Ilmenite-rich 100% Ilmenite	Ilmenite-rich Lherzolite+8% Ilm
H^* (kJ/mol)	86[a]	500[b]	275 − 325[c]	275 − 500[d]
Without inner core				
T_{lvz} (K)	>2,270	1,835±85	1,980±140	1,855±75
LVZ Density from Table 1 (kg/m^3)	3,884±300	3,884±300	3,884±300	3,884±300
Perple_X density (kg/m^3)	<3,200	<3,390	<3,380	<3,390
Possible overlap of density	N	N	N	N
With inner core				
T_{lvz} (K)	1,925±375	1,670±190	1,745±265	1,730±250
LVZ Density from Table 1 (kg/m^3)	3,559±94	3,559±94	3,559±94	3,559±94
Perple_X density (kg/m^3)	< 3,440	3,405±25	3,530±70	3,492±33
Possible overlap of density	N	N	Y	Y

Comparisons between geophysical constraints extracted from Table 1 and thermodynamical simulations using Perple_X. [a]Reference 25. [b]Reference 26. [c]Reference 13. [d]Putative values. The error bars are given at 2σ.

Extended Data Table 2 | Selenodetic observables used to constrain the modelled interior of the Moon

	Parameter	Value ± 2-σ	Reference
Mean radius (km)	R	1,737.1	[37]
Total mass (kg)	$M(\times 10^{22})$	7.34630 ± 0.00176	[32]
Moment of Inertia	C/MR^2	0.393112 ± 0.000024	[30]
Gravitational potential TLN	k_2	0.024059 ± 0.000352	[30]
Vertical displacement TLN	h_2	0.0386 : 0.0430	[38, 39]
Monthly quality factor	Q_F	38 ± 8	[32]
Yearly quality factor	$Q_{\ell'}$	41 ± 18	[32]

The Delaunay arguments F and ℓ′ correspond to periods defined by ref. 35 of 27.212 days and 365.260 days, respectively.

Extended Data Table 3 | Selenodetic 1D profiles used as inputs for interior modellings of the Moon

Layer	Radius	Density	Rigidity	Viscosity	Rheology
Unit	km	kg/m^3	$Pa \times 10^{10}$	log10(Pa·s)	
Crust	1,737.1	2,649	1.60	–	Elastic
Mantle	1,698.6	[3,300 : 4,000]	6.56	21	Maxwell
LVZ	[450 : 700]	[3,300 : 5,000]	2.48	[1 : 30]	Maxwell
Core	[100 : 450]	[4,000 : 15,000]	0	[1 : 30]	Newton
Outer core	[100 : 450]	[4,000 : 15,000]	0	[1 : 30]	Newton
Inner core	[100 : 350]	[4,000 : 15,000]	4.23	–	Elastic

General 1D profiles of the Moon interior used as intervals of possible values for the initialization of the random-walk Monte Carlo sampling. Values in brackets are parameters that vary randomly following a uniform distribution.

Extended Data Table 4 | LVZ characteristics

Symbol	Value	Unit	Reference
R	8.314,462	J· K^{-1} · mol^{-1}	–
H^*	86:500	kJ/mol	[6, 21, 22]
η_m	$1{\times}10^{21}$	Pa·s	this study
T_m	1,300:1,500	K	[34, 36]
With inner core			
z_m	1,195:1,254	km	this study
η_{lvz}	$3{\times}10^{16}$:$5{\times}10^{17}$	Pa·s	this study
Without inner core			
z_m	1,134:1,226	km	this study
η_{lvz}	$9{\times}10^{16}$:$1{\times}10^{20}$	Pa·s	this study

Parameters used for constraining the LVZ temperature.